

Article

Unmanned-Aircraft-System-Assisted Early Wildfire Detection with Air Quality Sensors [†]

Doaa Rjoub ¹, Ahmad Alsharoa ^{2,*} and Ala'eddin Masadeh ³¹ Civil Engineering Department, Missouri University of Science and Technology, Rolla, MO 65409, USA² Electrical and Computer Engineering Department, Missouri University of Science and Technology, Rolla, MO 65409, USA³ Department of Electrical and Electronics Engineering, Al-Balqa Applied University, Salt 19117, Jordan

* Correspondence: aalsharoa@mst.edu

[†] This paper is an extended version of our paper published in 2022 IEEE 96th Vehicular Technology Conference (VTC2022-Fall), London, UK, 26–29 September 2022.

Abstract: Numerous hectares of land are destroyed by wildfires every year, causing harm to the environment, the economy, and the ecology. More than fifty million acres have burned in several states as a result of recent forest fires in the Western United States and Australia. According to scientific predictions, as the climate warms and dries, wildfires will become more intense and frequent, as well as more dangerous. These unavoidable catastrophes emphasize how important early wildfire detection and prevention are. The energy management system described in this paper uses an unmanned aircraft system (UAS) with air quality sensors (AQSS) to monitor spot fires before they spread. The goal was to develop an efficient autonomous patrolling system that detects early wildfires while maximizing the battery life of the UAS to cover broad areas. The UAS will send real-time data (sensor readings, thermal imaging, etc.) to a nearby base station (BS) when a wildfire is discovered. An optimization model was developed to minimize the total amount of energy used by the UAS while maintaining the required levels of data quality. Finally, the simulations showed the performance of the proposed solution under different stability conditions and for different minimum data rate types.

Keywords: unmanned aircraft system; air quality sensors; optimization

Citation: Rjoub, D.; Alsharoa, A.; Masadeh, A. Unmanned-Aircraft-System-Assisted Early Wildfire Detection with Air Quality Sensors. *Electronics* **2023**, *12*, 1239. <https://doi.org/10.3390/electronics12051239>

Academic Editors: Sang Ik Han, Joobum Kim, Shiho Kim and Nurul I. Sarkar

Received: 5 February 2023
Revised: 25 February 2023
Accepted: 28 February 2023
Published: 4 March 2023



Copyright: © 2023 by the authors. Licensee MDPI, Basel, Switzerland. This article is an open access article distributed under the terms and conditions of the Creative Commons Attribution (CC BY) license (<https://creativecommons.org/licenses/by/4.0/>).

1. Introduction

1.1. Background

Millions of acres of forest are burned by wildfires every year, harming the environment, the economy, etc. In the last ten years, wildfires have become more severe and more frequent all across the world [1]. Over 8.7 million acres burned exclusively in the United States (U.S.) in 2018, costing about USD 24 billion in infrastructure damage and firefighting. Recent forest fires in the Western United States and Australia have consumed more than 50 million acres, engulfing many states [1]. For example, in 2020 alone, a Californian wildfire claimed 31 lives and burned more than 4.4 million acres [2]. Climate change is expected to increase wildfire severity and frequency in the future, as well as the risks associated with them [3]. Because of the speed with which wildfires spread, early detection is critical to keep flames under control and to extinguish them properly.

The traditional method of detecting wildfires makes use of lookout posts situated in highly visible regions [4–6]. When it comes to fire detection, this method is labor-intensive and has issues with worker safety [5,6]. Additionally, this approach can delay the detection of a fire (i.e, the worker may have been slow to notice or report the incident). Satellite remote sensing can also be used for monitoring forest fires and detecting wildfires [7]. It can identify active fires, evaluate scorched areas, and measure fire emissions [8,9]. In contrast, satellite imagery has a low spatial resolution (tens of meters) and requires an area without clouds, making it difficult to spot wildfires in their early stages [10]. Thermal imaging is

an additional method for detecting and monitoring fires and can be used to find hotspots throughout a fire's mapping and evolution [11]. Several initiatives in the United States and throughout the world attempt to install a huge set of thermal cameras in hotspot areas and forests. For example, the ALERTWildfire project in California has put three hundred fixed thermal cameras in Californian woods, with the intention of deploying around one thousand stations with superior cameras by 2022 [12]. Thermal cameras, on the other hand, have poor spatial resolution, are sensitive to weather, and may be affected by heavy vegetation, which blocks the thermal signal from a fire [11].

1.2. Related Works

The problem of estimating fire risk potential in a region has been investigated using machine learning algorithms, weights of evidence, and statistical index models [13,14]. For instance, the authors in [13] developed machine learning algorithms to investigate the effect of combining spatial and temporal parameters as a single combined dataset for estimating fire risk potential. To estimate fire risk potential, two models, the weights of evidence and the statistical index, were studied in [14]. On the other hand, other works focused on observing levels of pollution: in particular, tracers of wildfire pollutants such as particulate matter (PM) and carbon monoxide (CO) might be beneficial for identifying wildfire outbreaks [15]. AQSs are affordable and precise for the kinds of gases being looked at. AQSs typically function in three stages. In the first stage, the sensors scatter laser light to disperse particles into the air. In the subsequent second step, the sensors continuously record data on light scattering. The sensors' built-in microprocessors are then used to calculate particle levels, the corresponding particle sizes, and the quantity of particles of various sizes per unit volume in the final stage. Previous research revealed that conventional PM sensors have a limited detection limit. A sensor network can use a kriging interpolation method to map the spatiotemporal distribution of PM. On the other hand, it is simple to obtain CO sensors that can monitor CO content, since they are based on triboelectric nanogenerators, where these sensors have the advantage of using energy harvested from tree branch movement instead of using traditional batteries. However, if they are installed at fixed sites, a high number of sensors are required, which further complicates data transfer. This is one problem with using AQSs to detect wildfire. Furthermore, it is challenging to use these sensors in dangerous areas or in wooded areas.

Since they are inexpensive, require relatively low maintenance, are extremely mobile, and can cover large regions, even dangerous ones, unmanned aircraft systems (UASs) have emerged as a workable and realistic alternative for detecting forest fires and managing forests in general (i.e., they can function in areas that people cannot reach or are hidden from view) [16–21]. Previous research toward improving the wildfire detection framework has mostly focused on the use of thermal imaging [7,16,22–25]. These research works solved optimization problems in the pursuit of optimal positioning of the watchtower that reduced the expenses while maximizing the detection range. For example, in [7], the idea of constructing permanent watchtowers supported by high-definition video cameras and laser night vision was introduced to observe wildfires. More precisely, the authors formulated an optimization problem and solved it to determine the optimal watchtower sites that decreased the expenses while maximizing the detection range. Unfortunately, this proposed idea was both expensive and inflexible. The authors of [23] investigated the limitations and potential use of UASs equipped with thermal camera image intensifiers to detect and monitor wildfires. Despite the availability of a wide range of sensors with various capabilities for detecting infrared radiation, sensors face some challenges, including significant incident energy and reflected light during the day, the dynamic behavior of a burning flame, and the necessity of powerful computer vision algorithms. A vision-based UAS that analyzes captured images using motion and color attributes was suggested in [22]. They started their work by developing a color-based algorithm for identifying wildfires that uses the chromatic feature to obtain the fire-colored pixels. After that, they developed

flow algorithms to deal with the repercussions of the UAS's vibration on the resolution of the taken images.

Fire emission signatures, such as PM and CO, which are the predominant contaminants in fire emissions, may be measured using AQSs [26]. According to recent research, equipping UASs with AQSs might result in a faster responses to real-world fires [27,28], which creates a sensitive and early wildfire warning system [29]. Several research works looked at developing sensors that could assess both CO and PM levels [28,30]. For example, Wang et al. indicated that capturing CO and PM levels concurrently with active sampling increased the sensitivity of fire detection [28]. By combining CO and PM sensors with data processing algorithms, it is possible to distinguish between true and nuisance fire sources, resulting in a reduction in false alarms. The authors in [31] discussed utilizing large-scale Skywalker UASs with air quality sensors. The authors demonstrated how the use of UASs to measure pollution concentrations at the peri-urban scale/in peri-urban areas can give valuable extra indicator variability. This might result in more effective use of AQSs mounted on UASs for early wildfire sensing. As a result, building UASs with low-cost AQSs can help enhance wildfire sensing and treatment. Concerns about existing and proposed wildfire detection systems are compared in Table 1.

Table 1. Comparison between existing and introduced wildfire approaches.

Method	Concerns
Watchtowers [4–6]	Expensive labor. Workplace safety concerns. Prone to late detection of fires.
Satellite Remote Sensing [7–10]	Insufficient spatial resolution. The region being considered must be clear of clouds.
Thermal Imaging [11,12,23,24]	Insufficient resolution. There is some weather interference. Thick canopies may prevent the heat signal from the fire.
AQSs [28,30]	A vast number of sensors must be deployed in order to cover a broad region. Forests or dangerous places make deployment more difficult.
AQSs + UAS (proposed solution)	Limited capacity of the UAS battery. A base station is required for tracking and communication.

1.3. Main Contributions

Because of their ease of operation and widespread application in forest management, this article proposes integrating UASs with air quality sensors for wildfire detection. Further, the effectiveness of forest fire detection missions is primarily dependent on the UAS patrol algorithm, which controls the energy consumed by the UAS and the extent of area that can be covered [32]. The contributions of this paper are summarized as follows:

- We built an energy-efficient patrol UAS for early-stage forest fire detection. The UAS platform is equipped with PM, CO, and a radio transceiver, enabling data exchange with the BSs.
- We formulated and solved an optimization problem that minimizes the overall UAS energy consumption while accounting for the detection threshold, achievable data rate quality, transmit power budget cap, and the communication link associations between the UAV and BSs.
- We developed a powerful algorithm to maximize the area covered by forest patrols while enhancing the effectiveness of UAS patrols for accurate fire detection and data exchange.
- We propose a software protocol to manage the resource allocation between the UAS and the selected BS.

- To avoid an infeasible solution of the transmitted power, we introduced a data rate loss factor to prevent the case of insufficient transmitted power in satisfying the data rate QoS.

1.4. Outline

The paper is organized as follows. Section 2 presents the UAV–AQS integration system model. Section 3 shows the formulated optimization problem. Section 4 proposes the patrolling optimization solution. Section 5 proposes the data communication solution. Finally, the paper is concluded in Section 6.

2. System and Channel Model

We considered a single UAS that patrols a flat, rectangular area covered by a forests, as shown in Figure 1. The UAS is equipped with a radio transceiver that enables data interchange with one of the L nearby BSs in the event that a wildfire is discovered. We define θ_w as the direction of the wind in the area, with $\theta_w = 0$ serving as a reference for the north. AQSs on the UAS allow it to monitor PM ($\mu\text{g m}^{-3}$) and CO (ppm) levels.

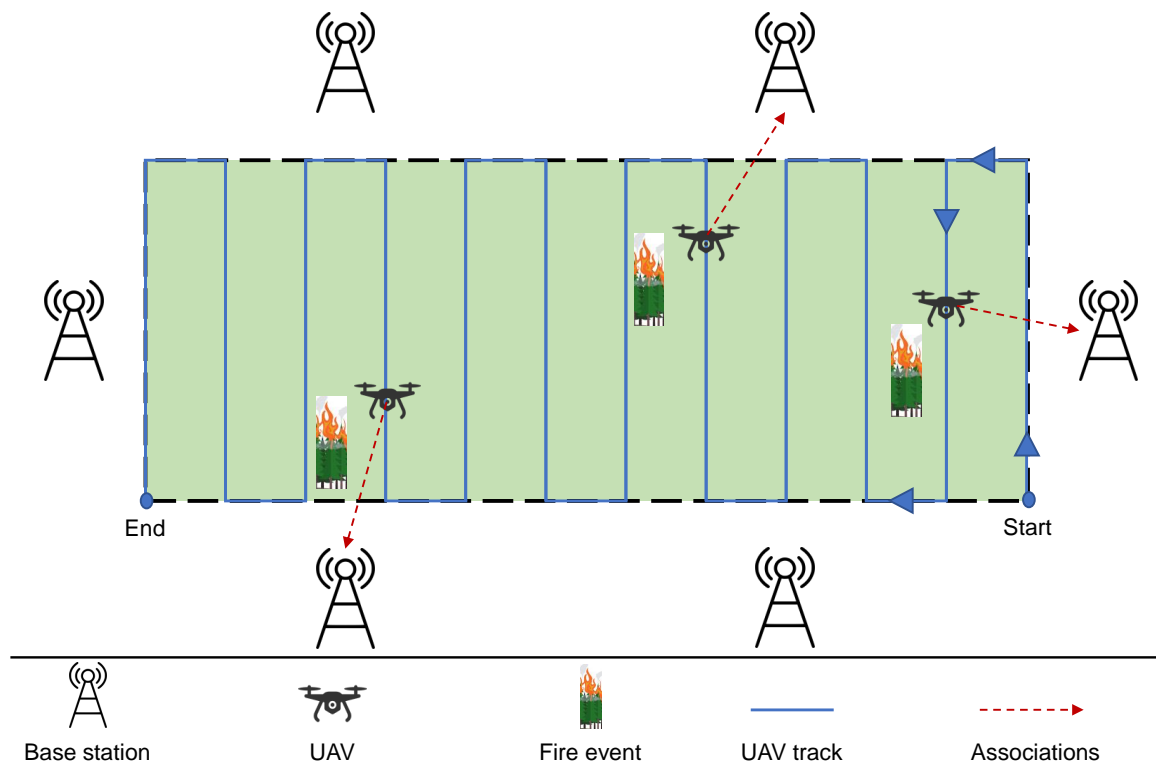


Figure 1. System model.

A wildfire incident is recognized if the measured concentrations of air pollutants by both sensors exceed the forest threshold backgrounds [33]. The UAS then sends real-time data to a chosen BS. As illustrated in Figure 2, an early-stage forest fire is occurring at a random point in the considered region and constantly releases PM and CO contaminants into the atmosphere via a plume that is carried by the air and scattered in all directions. Four parameters, which may be described as follows, were optimized for successful wildfire detection and reporting: (1) the UAS's altitude to guarantee that the UAS can pass through the plume; (2) the flight pattern of the UAS that ensures the UAS samples are in the plume for a considerable time; (3) the communication link between the UAS and the BSs; and (4) the transmission power utilized by the UAS to send the collected data to the BSs. These four factors have an impact on the UAS's battery, the amount of consumed energy, and hence, the overall area that the UAS can cover. In [13], Salavati et al. produced maps of

the fire hazard potential using statistical methods, where a number of reliable indicators were used to measure the likelihood of a fire. This can be very useful in our model in terms of distributing the UASs used and their path planning, where the probability of appearing can be increased over areas with high fire potential.

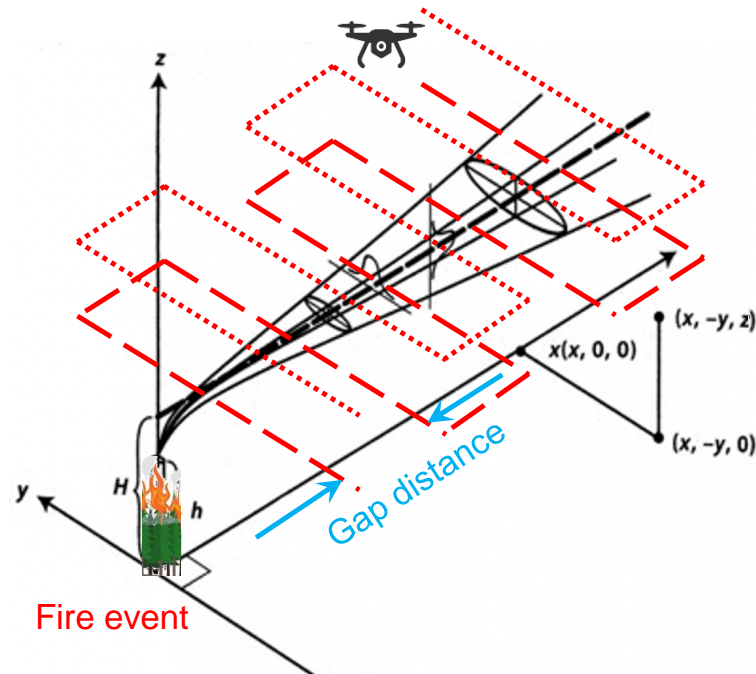


Figure 2. A Gaussian dispersion model for estimating the levels of air contaminants.

2.1. Pollutant Dispersion Model

Assuming the UAS travels at speed V , then $V\hat{T}$ represents the furthest distance it can travel in each time slot of length t , where \hat{T} represents the length of the time slot. Three-dimensional coordinates are used to show where the UAS is in relation to time t as $\hat{U}[t] = (x[t], y[t], z[t])$. As represented in Figure 1, the UAS is considered to be in a “Start Point” location at the beginning of the investigation and will land at the “End Point” spot once the inspection is completed. Dispersion models are frequently used to characterize the transfer of plumes [34].

The most-popular model for estimating the flow of air pollutants in a plume is the Gaussian dispersion model, as shown in Figure 1, making it feasible to measure the concentration of air pollution released from a source using the following mathematical formula [34]:

$$C(x, y, z) = \frac{Q}{2\pi u \sigma_y(x) \sigma_z(x)} \exp\left(-\frac{y^2}{2\sigma_y^2(x)}\right) \left[\exp\left(-\frac{(z-H)^2}{2\sigma_z^2(x)}\right) + \exp\left(-\frac{(z+H)^2}{2\sigma_z^2(x)}\right) \right] \tag{1}$$

where the horizontal and vertical spread parameters are denoted by $\sigma_y(x)$ and $\sigma_z(x)$, respectively, and depend on the distance x , as well as the stability of the surrounding atmosphere. C stands for the steady-state concentration at location (x, y, z) . Q stands for the emission rate. Pay attention to the fact that z denotes the vertical distance from the plume center line, u the average wind speed, and H the effective height of the emission point. The PM and CO indices will be denoted, for convenience, as $i = 1, 2$, respectively. The equivalent symbols for the sensor concentrations of CO and PM are C_1 and C_2 , respectively. The binary variable $\rho_i[t]$ is used to indicate whether the pollutant concentration i exceeds the cutoff $C_{th,i}$ during period t :

$$\rho_i[t] = \begin{cases} 1, & \text{if at time slot } t, C_i[t] \geq C_{th,i} \\ 0, & \text{otherwise.} \end{cases} \tag{2}$$

Define \bar{C}_i as the highest level of pollutant i 's concentration, that is the amount that can be precisely determined at the site of fire. By considering \bar{C}_i to represent the greatest concentration of the pollutant i , or the amount that can be precisely measured at the fire site, then we can re-write (2) as follows:

$$(C_{th,i} - C_i[t]) - \bar{C}_i(1 - \rho_i[t]) \leq 0, \quad \forall i, \forall t, \tag{3}$$

and

$$(C_i[t] - C_{th,i}) - \bar{C}_i\rho_i[t] \leq 0, \quad \forall i, \forall t. \tag{4}$$

It should be emphasized that, in order to describe (2) in a mathematical formula, both Constraints (3) and (4) must be used. Let us say $\rho[t]$ is set to 1 if both pollutants have concentrations over the concentration threshold, and $\rho[t]$ is set to 0 otherwise (i.e., at least one pollutant concentration is below the threshold).

2.2. UAS Communications Channel Model

Along with the line-of-sight signal, as indicated by [35], the BS may receive 2 distinct kinds of signals. Non-line-of-sight signals with strong reflections are the first kind, and fading signals with many reflections are the second. Both kinds of non-line-of-sight signals could be treated individually, with a distinct occurrence probability (i.e., the probability of line-of-sight occurrence) for each kind [35]. Several factors can influence the probability of occurrence, including the density, barrier diameters, and transmission elevation angles. In contrast to the line-of-sight signal and strongly reflected non-line-of-sight signals, the likelihood of multiple reflections is expected to be small [35,36]. Ground-to-air path loss (PL) modeling employing line-of-sight and non-line-of-sight components with their unique probabilities of occurrence is a typical technique for measuring the UAS to BS channel gain. That is to say, the channel gain is calculated as the weighted total of the two PLs' links (i.e., strongly reflected non-line-of-sight signals and a line-of-sight signal) [35,37]. For line-of-sight signal and strong reflected non-line-of-sight signals, the PL between the UAS and BS l located at \hat{U}_l can be expressed in this way [35,38,39]:

$$PL_l^{LoS}[t] = \zeta_{LoS} \left(\frac{4\pi\zeta_l[t]}{\lambda_0} \right), \tag{5}$$

$$PL_l^{NLoS}[t] = \zeta_{NLoS} \left(\frac{4\pi\zeta_l[t]}{\lambda_0} \right), \tag{6}$$

where $\zeta_l[t] = \|\hat{U}[t] - \hat{U}_l\|$ signifies the distance between the UAS and BS l and λ_0 is the signal wavelength. It should be noted that ζ_{LoS} and ζ_{NLoS} represent the additional shadowing losses for the line-of-sight signal and highly reflected non-line-of-sight signal propagation in free space, respectively. The line-of-sight probability is given by [40]:

$$p_l^{LoS}[t] = \frac{1}{1 + \nu_1 \exp(-\nu_2[\Theta_l[t] - \nu_1])}, \tag{7}$$

where $\Theta_l[t] = \frac{180}{\pi} \sin^{-1} \left(\frac{z[t]}{\zeta_l[t]} \right)$ denotes the elevation angle in degrees between the UAS and the BS. It should be noted that ν_1 and ν_2 are environment-dependent constant values. In light of this, the strong reflected non-line-of-sight probability is equal to $1 - p_l^{LoS}[t]$. Therefore, the average PL for a ground-to-air link is calculated using this PL model as follows:

$$PL_l[t] = p_l^{LoS}[t]PL_l^{LoS}[t] + (1 - p_l^{LoS}[t])PL_l^{NLoS}[t]. \tag{8}$$

Furthermore, the average gain of the channel connecting the UAS and the BS l over time slot t can be computed using

$$g_l[t] = \frac{1}{PL_l[t]}. \tag{9}$$

2.3. Data Transmission

When both PM and CO concentrations are above their respective concentration criteria, a wildfire is assumed to have occurred. To the designated BS, the UAS must therefore broadcast real-time data to it. The data kinds are divided into several $n = 1, \dots, N$ categories based on their QoS, which is expressed as a data rate threshold $R_{th,n}$ in bits/s. We assumed that, combined with AQSs, the UAS has a thermal camera that takes thermal images or videos, which provide precise 3D maps to increase the precision of the decisions. It is important to note that the QoS of the sensor output is different from the QoS of the thermal data with different QoSs and different data types. To represent the UAS–BS l communication connection over time period t , a binary variable $\epsilon_l[t]$ is defined. When BS l is connected to the UAS during time slot t , it equals 1; else, it equals 0, and it is given as

$$\epsilon_l[t] = \begin{cases} 1, & \text{if BS } l \text{ is connected to the UAS during time slot } t \\ 0, & \text{otherwise.} \end{cases} \quad (10)$$

When the concentrations of both pollutants are above the predetermined threshold (i.e., $\rho[t] = 1$), the main goal is to send all data kinds to the selected BS. As a result, the data rate of each kind n seeks to meet the threshold requirement as follows:

$$\rho[t]\epsilon_l[t] \left(B_0 \log_2 \left(1 + \frac{P_n[t]g_l[t]}{B_0N_0} \right) - R_{th,n} \right) \geq 0, \quad \forall n, \forall l, \forall t \quad (11)$$

where $P_n[t]$ and $g_l[t]$ are the UAS's transmission power assigned for data type n and the gain of the channel connecting BS l with the UAS during the t -th time slot, respectively. Note that B_0 and N_0 , respectively, stand for the frequency bandwidth and noise power. Constraint (11) states that the UAS must send all data types, thereby fulfilling the QoS requirement when a wildfire is discovered (i.e., $\rho[t] = \rho_1[t] \rho_2[t] = 1$), and when there is not a wildfire, it does not transmit (i.e., $\rho[t] = \rho_1[t] \rho_2[t] = 0$). That is to say, $\rho[t] = 1$ if both concentrations are greater than the threshold, and if one or more of the concentrations is less than the threshold, then $\rho[t] = 0$.

2.4. UAS Energy Model

In this context, the energy is consumed by the UAS for both flying and data transmission. The transmission power of UAS communication may be expressed as [41]

$$P_C[t] = \sum_{n=1}^N P_n[t], \quad (12)$$

where $P_C[t]$ and $P_n[t]$ denote, respectively, the total power of communication and the data type n transmission power of the UAS during the t -th time slot. Further, the UAS utilizes $P_F[t]$ flying and hovering power in addition to transmission power, given as [42]

$$P_F[t] = f(t) \left(\sqrt{\frac{(m_{\text{tot}}G)^3}{2\psi r_p^2 \omega_p \psi}} + P_s \right) \quad (13)$$

where P_s stands for the power used by the UAS equipment in Watts, ψ stands for air density in kilograms per cubic meter, and m_{tot} stands for the total mass of the UAS in kg. The parameters ω_p and r_p represent the number and radius of the UAS's propellers, respectively. The parameter $f(t)$ is an introduced binary variable that equals 1 if the UAS is flying during time t and 0 otherwise. As a result, the total amount of energy consumed can be stated as follows:

$$E_{\text{tot}} = E_F + E_C = \hat{T} \sum_{t=1}^T P_F[t] + \hat{T} \sum_{t=1}^T P_C[t]. \quad (14)$$

Note that, since $E_F \gg E_C$ (in contrast to transmission, which uses only fractional Watts of electricity, flight uses several Watts), the approximated total energy in (14) is provided by [41,42]

$$E_{tot} \approx E_F = \hat{T} \sum_{t=1}^T P_F[t], \quad (15)$$

where T is a dependent variable that has an impact on the overall amount of energy. Note that T becomes smaller and the energy is reduced if the UAS completes the patrol flying trip early. Even though $P_C[t]$ is significantly less than $P_F[t]$, it must be optimized since the transmitted power is crucial for achieving the data QoS specified in (11). The influence of $P_C[t]$ will be demonstrated in the problem solution and simulation results sections.

3. Problem Formulation

The problem of UAS patrols and communication is developed mathematically in this section. The goal is to minimize the total consumed energy and satisfy the detection threshold, data rate quality, budget for transmitting power, and the constraints of communication link associations for the UAS and BSs. Moreover, it was assumed that the UAS uses the OFDMA technology to simultaneously broadcast various data types over a range of bandwidths or frequencies.

The objective of the formulated optimization problem is to minimize the UAS's overall energy consumption over all time periods, while attempting to fulfill particular QoS for each type of data once a fire is detected. In addition, two complimentary sub-optimization problems are defined. The first one's objective is to identify the optimal UAS path inside the given region. The second optimization problem optimizes the communication link connecting the UAS with BSs, as well as the amount of power that the UAS uses to transmit each type of data when a wildfire is detected. We optimized the UAS's trajectory because the energy consumption rises as flight times increase. Further, due to the constrained capacity of the UAS battery, the UAS's traveling path limits the area that the UAS may patrol. For the sake of simplicity, let us suppose that the UAS follows a rectangular path, as depicted in Figure 3. The horizontal gap, a measurement between the two parallel legs, given by Δx has a substantial effect on the UAS's overall distance flown, according to this rectangular path. While a narrower gap results in longer flight distances and faster battery consumption, a larger spacing results in ineffective wildfire tracer detection and lower energy use. It should be noted that this rectangular track Δx that has been optimized can easily be modified to fit other shapes, such spiral or square. The rectangular track was chosen for its simplicity of use.

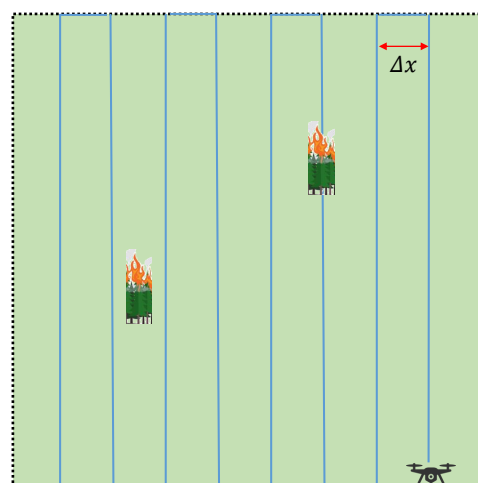


Figure 3. A graphical representation of the problem under consideration. The UAS patrol algorithm should be optimized to find the optimal flying path for detecting wildfires.

3.1. General Optimization Problem

Figure 4 depicts a profile of PM concentrations along parallel legs at various distances downstream of a fire occurrence, using an emission factor of 20 g/kg fuel [33]. Figure 4 also shows the profile of PM concentrations at various UAS heights (i.e., $z = 50\text{ m}$ $z = 100\text{ m}$). For example, when a PM measurement threshold of $75\ \mu\text{g m}^{-3}$ is used depending on three times the regulated concentration to recognize the fire incidence for $z = 50\text{ m}$ [34,43], only within 400 m downstream of the fire will PM concentrations exceed the threshold, as illustrated in Figure 4a. In other words, a UAS adopting a spacing greater than 400 m may miss the fire occurrence while on patrol. For $z = 100\text{ m}$, Figure 4b demonstrates that, if the UAS is not kept at an optimal height, it will be unable to detect the fire occurrence even 200 m downstream of the fire.

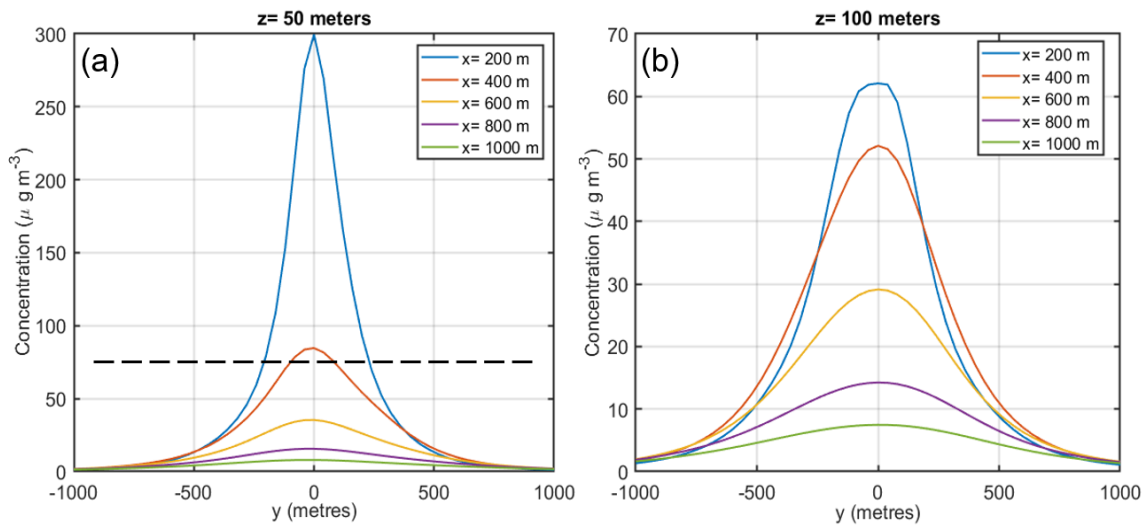


Figure 4. The profile PM concentrations are displayed along the y axis in the Gaussian dispersion model at various points (x) downstream of the emission site at altitudes (z) of (a) 50 m and (b) 100 m.

In this context, the maximum gap distance of the UAS is calculated using the Gaussian dispersion model. The longest distance the UAS could go and the size of the forest that could be patrolled are determined by the battery capacity of typical UASs. The overall optimization task seeks to minimize the energy used by the UAS over all time periods, while meeting specific QoS requirements when sensing wildfires. The variables of the optimization problem are: (i) the height of the UAS; (ii) the UAS pattern or horizontal gap; (iii) the communication link connecting the UAS with the BSs; and (iv) the transmission power assigned by the UAS to each type of data. Thus, the following formulation of the considered optimization problem may be provided as

$$\underset{(z[t], y[t], \Delta x, P_n[t]) \geq 0, (\rho_i[t], \epsilon_l[t]) \in \{0,1\}}{\text{minimize}} \quad E_{tot} \tag{16}$$

subject to

$$(C_{th,i} - C_i[t]) - C_{th,i}(1 - \rho_i[t]) \leq 0, \quad \forall i, \forall t \tag{17}$$

$$(C_i[t] - C_{th,i}) - \bar{C}_i \rho_i[t] \leq 0, \quad \forall i, \forall t \tag{18}$$

$$\rho[t] = \prod_{i=1}^2 \rho_i[t], \quad \forall t, \tag{19}$$

$$\rho[t] \epsilon_l[t] \left(B_0 \log_2 \left(1 + \frac{P_n[t] g_l[t]}{B_0 N_0} \right) - R_{th,n} \right) \geq 0, \quad \forall n, \forall l, \forall t, \tag{20}$$

$$\sum_{n=1}^N P_n[t] \leq \bar{P}, \quad \forall t, \quad (21)$$

$$\sum_{l=1}^L \epsilon_l[t] \leq 1, \quad \forall t, \quad (22)$$

where Constraints (17)–(19) make sure that, if a fire is recognized, the value of $\rho[t]$ will be set to one. The purpose of Constraint (20) is to ensure a specified QoS ($R_{th,n}$) for each type of data. Constraint (21) indicates a limitation of the transmission power due to the capabilities of the transmitters' hardware. Constraint (22) ensures that the UAS can only be linked to one BS over the time interval t . The two trajectory and communication sub-problems will be described in more depth in the sequel. Note that Constraints (17)–(22) are the set of conditions for the variables ($z[t], y[t], \Delta x, P_n[t], \rho_i[t], \epsilon_l[t]$) that are required to be satisfied. This can be reflected by the objective function. The goal is to find a feasible unique solution at an intersection of the constraints. Due to the non-convexity of the problem, in the sequel, we formulate two sub-optimization problems for trajectory and data transmission optimization.

3.2. Trajectory Optimization

To efficiently identify the occurrence of a fire in its early stages, we optimized the UAS's height and trajectory. The patrolling optimization sub-problem can therefore be written as

$$\underset{(z[t], y[t], \Delta x, \rho_i[t], \epsilon_l[t]) \geq 0}{\text{minimize}} \quad E_{tot} \quad (23)$$

subject to

$$C(x = \Delta x, y[t], z[t]) \geq C_{th,i}, \quad \forall i, \quad (24)$$

When a fire breaks out in the area of concern, $z[t]$ considers meeting $C_{th,i}$ for both PM and CO pollutant types. Constraint (24) is utilized to ensure that the horizontal distance is Δx . This will make sure that any wildfires are found in the area of interest. The $\rho[t]$ value will be based on the real-time concentration readings from the PM and CO sensors.

3.3. Data Transmission Optimization Problem

This section defines the data transmission sub-problem while taking into account the QoS restriction stated in (20) when a fire is discovered, or when $\rho[t] = 1$. As a result, the communication sub-problem used to maximize the UAS transmission power for various data types and associations $\epsilon_l[t]$ is as follows:

$$\underset{P_n[t] \geq 0, \epsilon_l[t] \in \{0,1\}}{\text{minimize}} \quad E_{tot} \quad (25)$$

subject to (20)–(22).

4. UAS Patrolling Solution

The sub-problem of the UAS patrolling optimization is presented in this section with a suggested solution. To maximize the UAS patrols' coverage area and to take into account the UAS's battery constraints, this part optimizes the UAS's flight path using a plume dispersion model to find the types of gases produced by a wildfire. This part also provides findings from Monte Carlo simulations to support the viability of the solution.

4.1. UAS Patrolling Algorithm

To effectively locate early-stage fire occurrences, the UAS must cross the plume at its centerline, $z[t] = H$, at the height of the plume. The equation that is used to calculate H is expressed as [34]

$$H = h_0 + \frac{v_s d_s}{u} \left[1.5 + 2.68 \times 10^{-2} P_a \left(\frac{K_s - K_a}{K_s} \right) d_s \right] \quad (26)$$

where d is the diameter at the emitting point, h_0 is the elevation of the burning plume, v_s is its upward velocity, P_a is its pressure, K_s is its temperature, and K_a is the temperature of the air around it. Additionally, the peak incidence will occur at $y = 0$ according to the Gaussian dispersion model, as shown in Figure 4. Therefore, the optimal or maximum horizontal spacing distance Δx for rectangular UAS motion is calculated based on the surrounding environment and the information that is currently available about fire plumes [44]. As depicted in Figure 3, by finding the solution of the subsequent optimization problem, notice that the minimization of E_F is on an equal footing with the maximization of Δx :

$$\underset{\Delta x}{\text{maximize}} \quad \Delta x \quad (27)$$

subject to

$$C(x = \Delta x, y = 0, z = H) \geq C_{th,i} \quad \forall i, \quad (28)$$

where Constraint (28) ensures that the horizontal distance Δx meets $C_{th,i}$ for all polluting types (i.e., PM and CO). Constraints (27) and (28) are non-convex and non-linear. As a result, determining the best solution is difficult [45]. We propose using a meta-heuristic technique based on the Genetic Algorithm (GA) to identify a nearly optimal path for patrolling horizontal gaps because of its quick deployment and short convergence time [46]. The foundation of this method is natural random evolution. The GA begins by randomly selecting a population with a predetermined number of strings. Strong strings survive generation after generation of the algorithm, whereas weak strings perish. After that, the GA uses mutation and crossover processes to create new strings from the surviving ones. It should be noted that the crossover process involves randomly splitting two surviving parent strings and swapping the acquired pieces to create two new strings. The mutation operator, on the other hand, is used to update a random string value with a specific probability [47].

4.2. Patrolling Simulation Results

This section presents selected experimental results to demonstrate the advantages of the proposed patrolling strategy. We considered the reference emission rates $Q_{0,i}$ of PM and CO that follow Gaussian distributions $\mathcal{N}(17.4, 7.2)$ and $\mathcal{N}(64.5, 16.7)$ [33]. $C_{th,1}$ and $C_{th,2}$ were assumed to be $75 \mu\text{g m}^{-3}$ and 150 ppm, respectively (in light of three-times the controlled concentration to identify the fire occurrence) [34,43]. Table 2 summarizes the remaining simulation settings [34,48,49]. Four stability scenarios (extremely unstable, moderately unstable, slightly unstable, and neutral) were considered (1). Note that σ_y and σ_z were determined and given, respectively, in light of a reasonable approximated fit as [34]

$$\sigma_y = ax^b, \quad (29)$$

$$\sigma_z = cx^d + f, \quad (30)$$

where the parameters a, b, c, d, f are listed in Table 3 [34]. Figures 5–7 show examples of a 2D Gaussian pollutant concentration dispersion model in a plume for extremely unstable, slightly unstable, and neutral atmospheric stability conditions.

Table 2. The parameters used in the simulation.

Constant	Value	Constant	Value	Constant	Value
V (m/s)	5	h_0 (m)	15	v_s (m/s)	1.55
d_s (m)	4.75	K_a (K)	308.15	K_s (K)	1106.15
P_a (mb)	1000	P_s (W)	0.5	m_{tot} (kg)	1
ψ (kg/m ³)	1.225	ω_p	4	r_p	0.2

Table 3. Stability coefficients based on the Gaussian dispersion model.

Stability	a	b	$\Delta x \leq 1$ km			$\Delta x > 1$ km		
			c	d	f	c	d	f
1—Very unstable	213	0.894	440.8	1.941	9.27	459.7	2.094	−9.6
2—Moderate unstable	156	0.894	106.6	1.149	3.3	108.2	1.098	2.0
3—Slightly unstable	104	0.894	61.0	0.911	0	61.0	0.911	0
4—Neutral	68	0.894	33.2	0.725	−1.7	44.5	0.516	−13.0

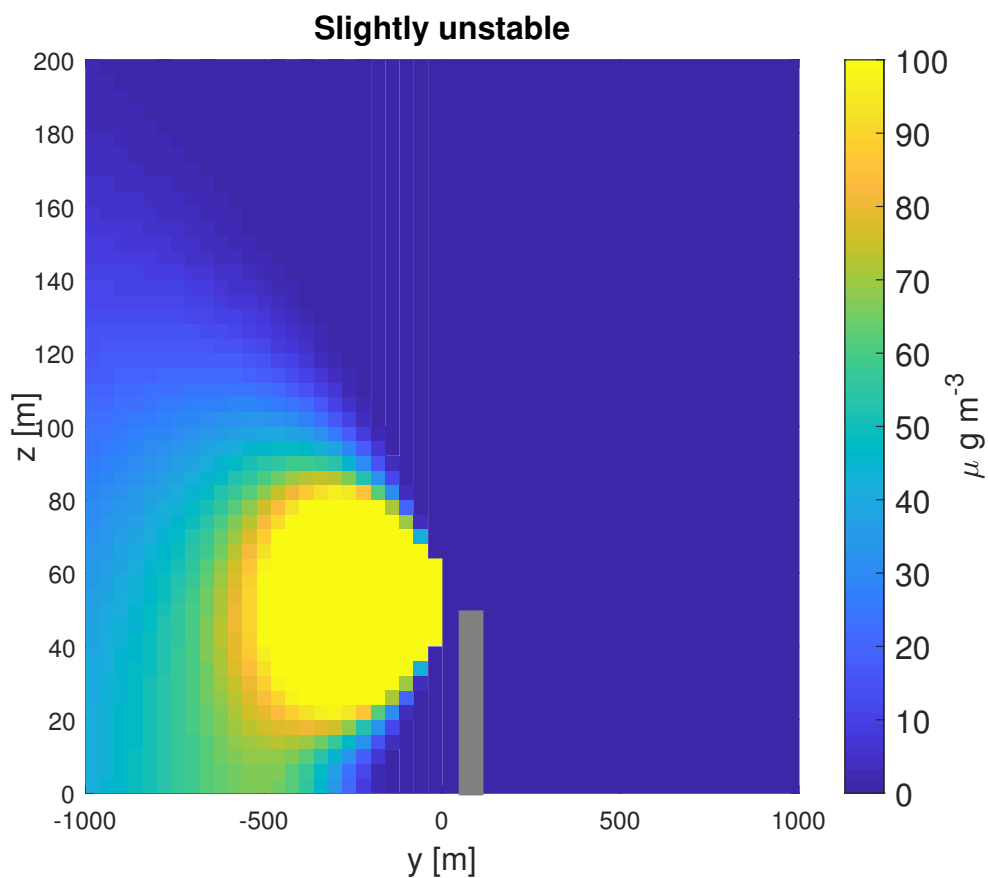


Figure 5. The 2D Gaussian pollutant concentration dispersion model in a plume for the slightly stable situation. The gray bar represents the effective height of the emission point.

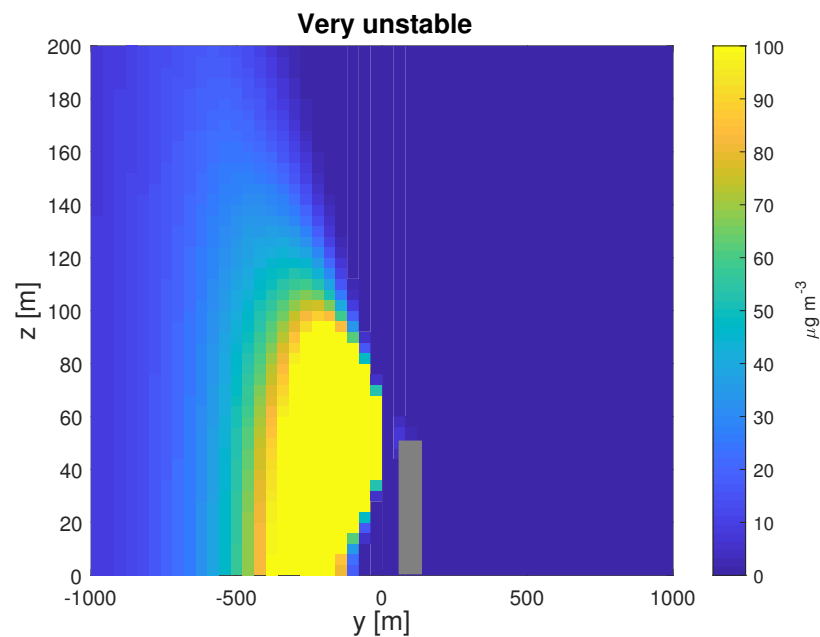


Figure 6. The 2D Gaussian pollutant concentration dispersion model in a plume for the very/extremely unstable situation. The gray bar represents the effective height of the emission point.

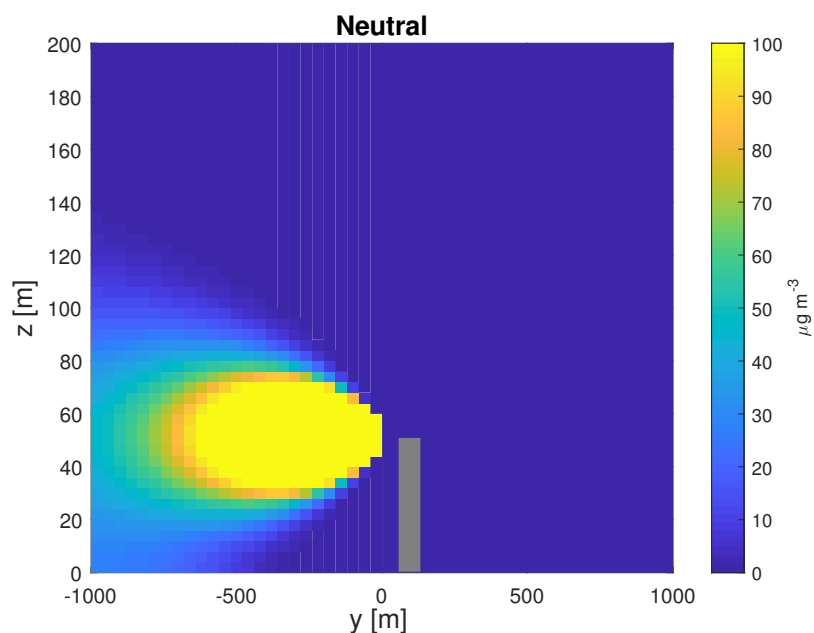


Figure 7. The 2D Gaussian pollutant concentration dispersion model in a plume for the neutral stability situation. The gray bar represents the effective height of the emission point.

The horizontal gap Δx as a function of the wind speed u is depicted in Figure 8. It is shown that, as the wind speed increases, the horizontal gap between all of the various stability factors decreases. This is because of the inverse proportional relationship between the pollutant concentration C and the wind speed u , as shown in (1). It is worth noting that, as C rises at the same position (x, y, z) , Δx rises as well, because the UAS can detect the C_{th} beyond this point. At low wind speeds, the differences between various types of stability conditions are significant. When $u = 2$ m/s, for example, Δx for the neutral and severely unstable conditions is approximately 220 m and 160 m, with an estimated difference of 80 m. When $u = 20$ m/s, Δx for the neutral and severely unstable conditions is approximately 900 m and 400 m, with a 500 m difference. The distance between the

various stability scenarios narrows as u rises. When $u = 20$ m/s, Δx for the neutral and severely unstable conditions is approximately 900 m and 400 m, with a 500 m difference. The distance between the various stability scenarios narrows as u rises.

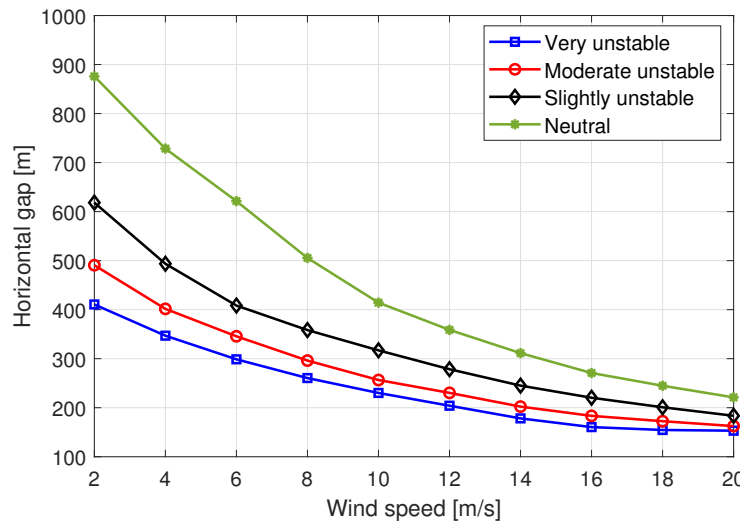


Figure 8. The horizontal gap for various stability situations as a function of wind speed.

Figure 9 shows the relationship between the horizontal gap Δx and the emission rate factor κ . The parameter κ is used to represent the emission rate in terms of the reference emission rate, as specified by the formula $Q_i = \kappa_i Q_{0,i}, \forall i = \{1, 2\}$. The symbols κ_1 and κ_2 represent the emission rate factors for PM2.5 and CO, respectively. This can show how increasing or decreasing the emission rates affects the horizontal gap. The horizontal gap grows as κ increases for the same emission rate factor $\kappa = \kappa_1 = \kappa_2$, according to Figure 9. As a result, the proportional relationship between C and Q (1) was validated. As a result, as Q rises, as does Δx .

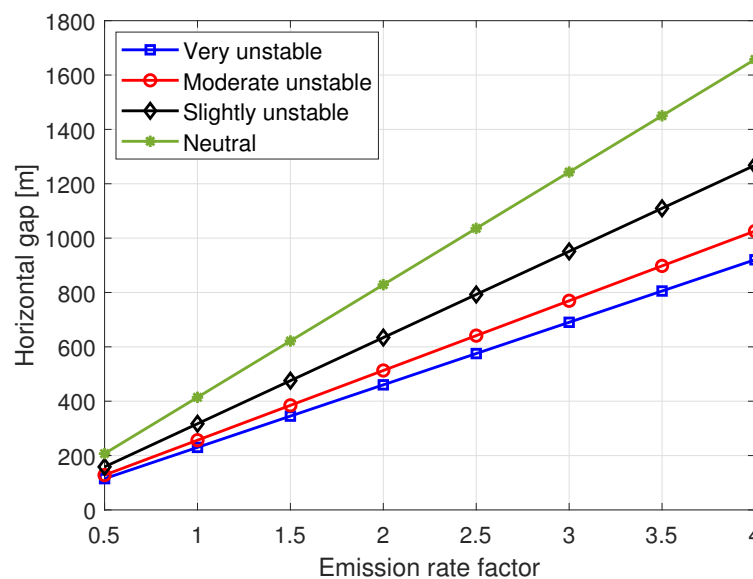


Figure 9. The horizontal gap versus the emission rate factor for various stability situations.

Figures 10 and 11 show the horizontal gap Δx for the highly unstable and neutral conditions by fixing one emission rate component and changing the other. For example, in Figure 10, we vary κ_1 while keeping κ_2 constant for both the extremely unstable and

neutral conditions. To put it another way, the Q_1 values change, but Q_2 remains constant. For low κ_1 values, the PM pollutant dominates the optimization of Δx up to the cut-off point, that is about 1.5 for a very unstable environment and 1.25 for a neutral condition. The CO pollutant thus becomes the key element in optimizing Δx . Figure 11 investigates the effect of changing κ_2 and keeping κ_1 constant for both the highly unstable and neutral conditions. That is, the rate of CO emissions varies while the rate of PM2.5 emissions remains constant. In this scenario, the study produced various cutoff points (i.e., approximately 0.5 for extremely the unstable conditions and 0.8 for the neutral conditions).

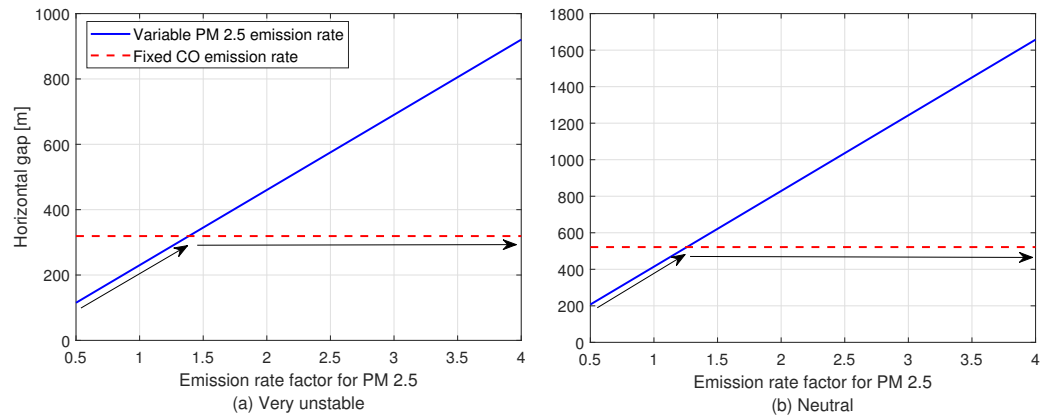


Figure 10. The impact of the PM2.5 emission rate on the horizontal gap while keeping the CO emission rate constant. The black arrow indicates the chosen optimal value of the horizontal gap when the PM2.5 pollutant’s rate factor is changed while the CO pollutant’s rate remains constant.

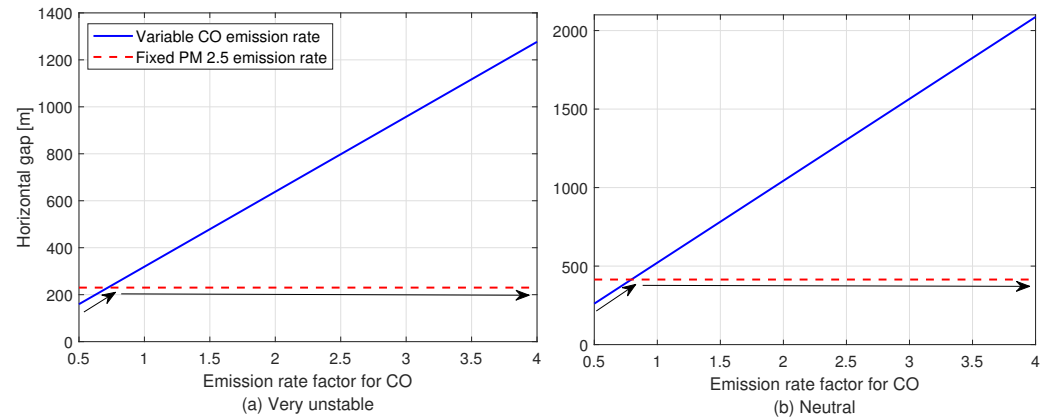


Figure 11. The impact of the CO emission rate on the horizontal gap while keeping the PM2.5 emission rate constant. The black arrow indicates the chosen optimal value of the horizontal gap when the CO pollutant’s rate factor is changed while the PM2.5 pollutant’s rate remains constant.

Figure 12 depicts the estimated rectangular area that a UAS with a speed of $V = 5 \text{ m/s}$ can patrol as a function of the horizontal gap for various battery capacities. It was demonstrated that, as the horizontal gap grows, so does the patrolled area. For instance, with a horizontal gap of $\Delta x = 500 \text{ m}$, the UAS can scan regions of around 1 km^2 and 3.2 km^2 using batteries having capacities of 6 KJ and 24 KJ , respectively.

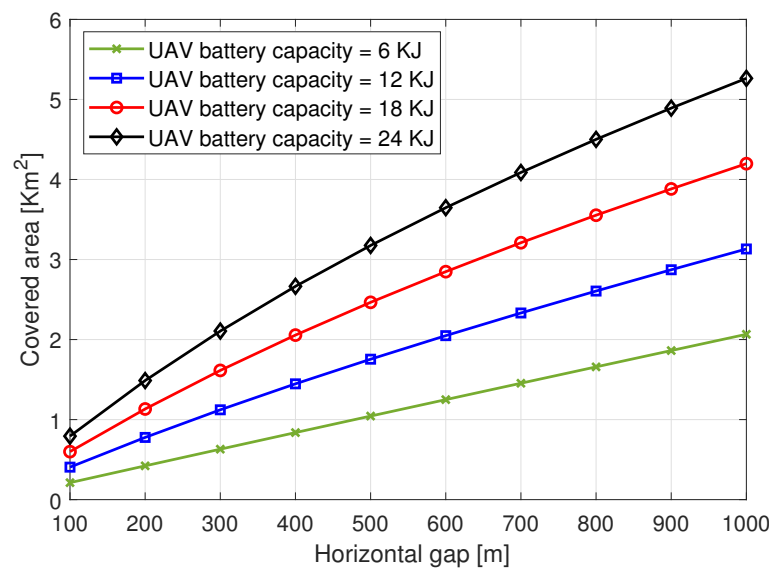


Figure 12. The area covered by the UAS as a function of the horizontal gap for various UAS battery limitations.

5. Data Communication Solution

This section provides the solution to the UAS communication sub-problem. For each data type, the communication resources are optimized in this section to meet the target data rate QoS. The communication resources consists of the UAS transmission power and the communication link between the UAS and the BSs. This section also provides a software design management protocol for managing resource allocation between the UAS and the chosen BS. The section presents the simulation findings that support the reliability of the proposed solution to the communication problem.

5.1. UAS–BS Protocol

In the proposed protocol, the UAS implements a software management protocol that governs transmission power allocation, UAS-to-BS connections, and the trajectory of the UAS. It should be noted that a control link is required between the BSs and the UAS. As a result, creating a UAS–BS link is necessary (i.e., this part is solely reserved for protocol management). The following is a brief explanation of a basic management protocol that manages the link between the BS and UAS in this paper.

5.2. Establishment of the UAS–BS Link

To establish a communication link between the designated BS and UAS, each BS broadcasts a UASSEARCH frame on a regular basis. The UAS collects the UASSEARCH frame from adjacent BSs and analyzes the levels of contaminants. All BSs are added by the UAS to the list of potential BSs. If the pollution levels are below a specific threshold C_{th} , the UAS disregards these frames; if not (i.e., for both pollutants $C_i[t] \geq C_{th}$, $i = 1, 2$), the UAS sends a UASACK packet to the list of all potential BSs that contains the Ethernet/MAC addresses of the UAS. In the event of many UASs (which might be an extension of this paradigm), it should be noted that the BSs may receive several UASACK frames from various UASs. If this occurs, a collision protocol should be employed to prevent collisions caused by several UASACKs arriving at the BSs at once. We assumed that there is a central unit that connects all BSs using optical fibers, so, when the BSs receive the UASACK frame, the central unit chooses the optimal BS to interact with the UAS. After that, the chosen BS communicates with the UAS and controls the transmission power assigned to each data type, thereby instructing the UAS to transmit the data over the available bandwidth resources using the optimal transmission power.

5.3. Maintenance of the UAS–BS Link

When a communication link is created between the specified BS and the UAS, the UAS is added to the “UAS table” of that BS. The table is updated on a regular basis by delivering UASSEARCH-UASACK signals, as explained in the UAS–BS link setup.

5.4. Termination of the UAS–BS Link

When the UAS fails to respond to the BS with a UASACK due to particular reasons (for instance, when the UAS is out of range or measures a pollutant concentration less than the threshold), the “UAS table” of the BS will be updated. With this update, the UAS is no longer in the table. The termination options include the following: (1) graceful leave, in which the UAS notifies the BS in advance about terminating via the CLOSE frame; this could be due to a number of potential causes, such as the UAS’s battery being depleted or the pollution levels being below the threshold; (2) ungraceful leave, in which the UAS cuts off the communication without alerting the BS. In this situation, the BS keeps sending timeout-based UASSEARCH packets. This indicates that the maximum number of UASSEARCH frames has been reached without a response, so the communication will be terminated. It should be noted that the maximum number of UASSEARCH frames can be chosen depending on the scenario or application.

5.5. Communication Optimization Solution

In order to fulfill the QoS constraint stated in (20) when a wildfire is identified, the data transmission optimization problem is defined in this subsection. Indeed, due to the limited transmission power circuit or the instability of the communication channel gain over time, this can be a difficult condition to fulfill in practice at all time slots. To keep the problem from being impractical (i.e., inability to satisfy the needed QoS with the budgeted transmission power resources), we define a fraction variable called the “loss factor”, σ , to relax $R_{th,n}$, as shown in

$$B_0 \log_2 \left(1 + \frac{P_n[t]g_l[t]}{B_0N_0} \right) \geq R_{th,n} - \sigma[t]R_{th,n}. \tag{31}$$

where $\sigma[t]$ ($0 \leq \sigma[t] \leq 1$) indicates the rate’s loss factor for the time slot t . For instance, if $\sigma[t] = 0.2$, the attainable data rate will be reduced by a factor of 0.2. Similarly, when $\sigma[t] = 0$, $R_{th,n}$ can be obtained. As a result, the objective is to minimize $\sigma[t]$ to come as close to $R_{th,n}$ as possible. The following optimization problem is expressed instantly (that is, for each time slot t) as follows:

$$\underset{\rho_i[t], P_n[t], \epsilon_l[t], \sigma[t]}{\text{minimize}} \quad \sigma[t] \tag{32}$$

subject to

$$\rho[t] = \prod_{i=1}^2 \rho_i[t], \tag{33}$$

$$\rho[t]\epsilon_l[t] \left(B_0 \log_2 \left(1 + \frac{P_n[t]g_l[t]}{B_0N_0} \right) - (R_{th,n} - \sigma[t]R_{th,n}) \right) \geq 0, \quad \forall n, \forall l, \tag{34}$$

$$\sum_{n=1}^N P_n[t] \leq \bar{P}, \tag{35}$$

$$\sum_{l=1}^L \epsilon_l[t] \leq 1, \tag{36}$$

$$\sigma[t] \leq 1, \tag{37}$$

where Constraint (37) ensures that the maximum loss tolerance is 1.

5.6. Data Transmission Optimization Solution

The problem defined in (32)–(37) is a mixed-integer non-linear optimization problem due to the presence of binary variables $\rho_i[t]$ and $\epsilon_l[t]$ [45]. The specified optimization issue was simplified by our three-step solution process. First, we determined $\rho_i[t]$ by comparing the concentration of each pollutant species to the threshold value. Second, the optimal channel gain between the UAS and BSs was chosen, as described in the UAS–BS protocol section. Finally, the problem was transformed into a convex optimization problem for $P_n[t]$ and $\sigma[t]$, where the optimum values of transmission power ($P_n[t]$) and loss tolerance ($\sigma[t]$) were determined by exploiting the strong duality [45]. Therefore, for a given $\rho_i[t]$ and $\epsilon_l[t]$, the communication optimization problem defined in (32)–(37) will be

$$\underset{P_n[t], \sigma[t] \geq 0}{\text{minimize}} \quad \sigma[t] \tag{38}$$

subject to (34), (35), (37).

It should be noted that the above optimization problem presented is convex due to the convexity of the domain, the linearity of the objective function (i.e., convex function), and the convexity of all the inequality constraints. We used the Lagrangian approach [45] to obtain the optimal transmission power. Therefore, the Lagrangian is given as follows:

$$\begin{aligned} \mathcal{L}(\lambda_{1,n}, \lambda_2, \lambda_3, P_n[t], \sigma[t]) = & \\ \sigma[t] + \sum_{n=1}^N \lambda_{1,n} \rho[t] \epsilon_l[t] \left((R_{th,n} - \sigma[t] R_{th,n}) - B_0 \log_2 \left(1 + \frac{P_n[t] g_l[t]}{B_0 N_0} \right) \right) & \\ + \lambda_2 \left(\sum_{n=1}^N P_n[t] - \bar{P} \right) + \lambda_3 (\sigma[t] - 1). & \end{aligned} \tag{39}$$

In (39), the vector λ includes all of the system’s Lagrangian multipliers, where the Lagrangian multipliers related to the QoS for data n , peak power, and loss tolerance constraints are denoted by $\lambda_{1,n}$, λ_2 , and λ_3 , respectively. By considering the Lagrangian derivative, given in (39), with respect to $P_n[t]$ and $\sigma[t]$, the optimal transmission power and optimal may be calculated as follows:

$$P_n[t] = B_0 \left(\frac{\lambda_{1,n} \rho[t] \epsilon_l[t]}{\lambda_2 \ln(2)} - \frac{N_0}{g_l[t]} \right)^+, \quad n = 1, \dots, N. \tag{40}$$

$$1 + \lambda_3 = \lambda_{1,n} \rho[t] \epsilon_l[t] R_{th,n}, \quad n = 1, \dots, N. \tag{41}$$

where $(x)^+ = \max(x, 0)$. Note that finding the optimal Lagrangian multipliers for this problem can be achieved by using the subgradient method, the ellipsoid method, or other heuristic techniques [50].

5.7. Communications Simulation Results

For the purpose of demonstrating the communication solution, this subsection gives the simulation results. Assuming that $n = 3$, different $R_{th,n}$ were used, such as $R_{th,1} = 1$ Mbits/s (for a poor QoS data rate), $R_{th,2} = 5$ Mbits/s (for a medium QoS data rate), and $R_{th,3} = 10$ Mbits/s (for a high QoS data rate).

Figures 13 and 14 validate the effectiveness of the data transmission. For three different types of data rate requirements, Figure 13 illustrates the average attainable data rate: (1) Type 1 is appropriate for applications with low data rate needs, such as sensor readings; (2) Type 2 is appropriate for medium data rate needs, such as low-resolution data or thermal imaging; (3) Type 3 is appropriate for high data rate needs, such as for high-resolution data or videos. It should be noted that the communications data rate is dependent on the transmission power and loss tolerance of the UAS, as stated in (34). Figure 13 demonstrates that, up to a certain value, the possible throughput increases as the power budget \bar{P} increases. This is because, once \bar{P} reaches this value, the transmission data rate threshold is met, negating the need to use further energy. Figure 13 also demonstrates that $R_{th,n}$ may

not be attained if the transmission power budget \bar{P} is low. This could be caused by the shadowing effect, PL , or state of the communication channel. However, when \bar{P} is large (for example, 40 dBm W), the loss is negligible and $R_{th,n}$ can be attained.

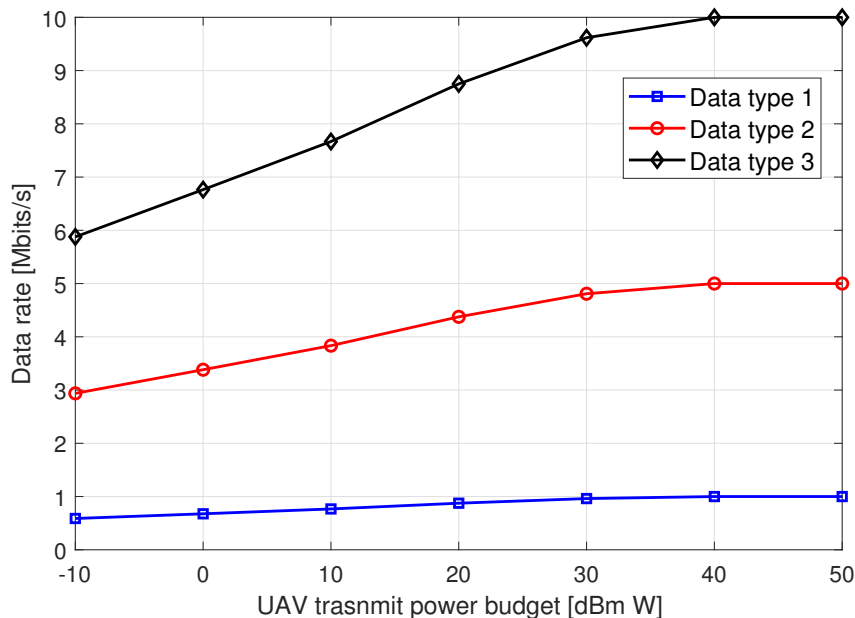


Figure 13. Average data rate attained in relation to UAS transmit power budget.

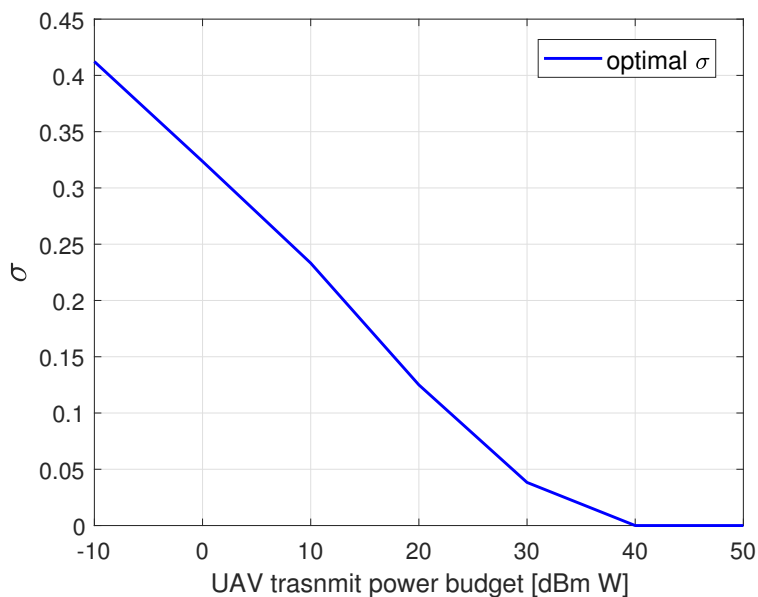


Figure 14. Loss tolerance as a function of UAS transmit power budget.

On the contrary, Figure 14 depicts the average loss tolerance as a function of the power budget \bar{P} . It depicts the amount of loss in the desired rate threshold against the power budget \bar{P} of the UAS. As an illustration, if $\bar{P} = 10$ dBm W (i.e., 0.01 W), the average loss in the rate is around $0.23R_{th,n}$ for each data type n .

Table 4 gives examples of the transmission power P_n , data rate R_n , and loss tolerance σ for each of the three data types and various power budgets \bar{P} . This table verifies the analysis that, when \bar{P} is low, the transmission power optimization problem optimizes the transmission power with the goal of reducing the loss tolerance σ . For instance, for Data Type 2, utilizing $\bar{P} = 1$ W rather than $\bar{P} = 0.1$ W reduces the optimal σ from 0.125 to 0.038 and increases the data rate R_2 from 4.38 Mbits/s to 4.8 Mbits/s.

Table 4. Power budget and loss factors are determined using various UAS power budgets.

Data Type	$\bar{P} = 0.1 \text{ W}$			$\bar{P} = 1 \text{ W}$		
	σ	R_n (Mbits/s)	P_n (W)	σ	R_n (Mbits/s)	P_n (W)
1	0.125	0.87	0.016	0.038	0.96	0.29
2	0.125	4.38	0.019	0.038	4.80	0.31
3	0.125	8.75	0.065	0.038	9.62	0.40

6. Conclusions

This paper developed a novel method for merging UASs with air quality and communication transceivers with the goal of detecting wildfires early. By quickly identifying pollutants, pinpointing the source of the fire, and offering more details about pollutants' dispersion, this proposed framework can perform better than thermal imaging and other existing approaches. Additionally, the idea of autonomous patrol optimization (i.e., optimizing the UAS's flying path) can successfully detect wildfire occurrences while preserving the UAS's battery for a larger coverage area. The goal was to solve the UAV's trajectory and data communication optimization. The trajectory problem was solved using heuristic approach based on the GA. The data communication problem was transformed to a convex optimization problem and solved by regular convex optimization methods. Further, we introduced a rate loss factor to ensure the feasibility of the problem. Future and ongoing studies will use innovative methods to create fresh tactics that will improve the performance of such systems. Future suggestions include looking into other wildfire hotspot zones. It is worthwhile to have the UAS patrol above these hotspot zones in spirals or other motion patterns after identifying these places using historical data. This will result in greater track complexity and increased UAS energy consumption.

Author Contributions: The following specify the individual contribution of the authors. D.R.: literature search, figures, tables, system model discussion, problem formulation and solution, data analysis, data interpretation, and writing. A.A.: system model discussion, problem formulation and solution, data analysis, data interpretation, and writing. A.M.: system model discussion, data analysis, data interpretation, and writing. All authors have read and agreed to the published version of the manuscript.

Funding: This research received no external funding.

Data Availability Statement: No data were created.

Conflicts of Interest: The authors declare no conflict of interest.

References

1. Kolaric, D.; Skala, K.; Dubravic, A. Integrated System For Forest Fire Early Detection and Management. *Period. Biol.* **2008**, *110*, 205–211.
2. US Today. Two Dead Near Los Angeles as Saddleridge Fire Forces 100,000 People to Evacuate. Available online: <https://www.usatoday.com/story/news/nation/2019/10/11/california-saddleridge-fire-spreading-evacuations-power-outages/3941274002/> (accessed on 27 February 2023).
3. Center for Climate and Energy Solutions. Record Wildfires Push 2018 Disaster Costs to \$91 Billion. 2019. Available online: <https://www.c2es.org/2019/02/record-wildfires-push-2018-disaster-costs-to-91-billion/> (accessed on 27 February 2023).
4. Rego, F.; Catry, F. Modeling the effects of distance on the probability of fire detection from look outs. *Int. J. Wildland Fire* **2006**, *15*, 197–202. [CrossRef]
5. Matthews, S.; Sullivan, A.; Gould, J. Field evaluation of two image-based wildland fire detection systems. *Fire Saf. J.* **2012**, *47*, 54–61. [CrossRef]
6. Murray, A. Optimising the spatial location of urban fire stations. *Fire Saf. J.* **2013**, *62*, 64–71. [CrossRef]
7. Bao, S.; Xiao, N.; Lai, Z.; Zhang, H.; Kim, C. Optimizing watchtower locations for forest fire monitoring using location models. *Fire Saf. J.* **2015**, *71*, 100–109. [CrossRef]
8. NASA. Techniques for Wildfire Detection and Monitoring. Available online: <https://appliedsciences.nasa.gov/join-mission/training/english/arset-techniques-wildfire-detection-and-monitoring> (accessed on 27 February 2023).

9. Environment and Natural Resources. Detecting Wildfire. Available online: <https://www.enr.gov.nt.ca/en/services/wildfire-operations/detecting-wildfire> (accessed on 27 February 2023).
10. Gao, Z.; Zhang, L.; Li, X.; Liao, M.; Qiu, J. Detection and analysis of urban land use changes through multi-temporal impervious. *J. Remote Sens.* **2010**, *14*, 593–606.
11. Pardo, J.; Aguilar, W.; Toulkeridis, T. Wireless communication system for the transmission of thermal images from a UAV. In Proceedings of the 2017 CHILEAN Conference on Electrical, Electronics Engineering, Information and Communication Technologies (CHILECON), Pucon, Chile, 18–20 October 2017; pp. 1–5.
12. ALERTWildfire. ALERTWildfire Project. Available online: <https://www.alertwildfire.org/> (accessed on 27 February 2023).
13. Salavati, G.; Saniei, E.; Ghaderpour, E.; Hassan, Q.K. Wildfire Risk Forecasting Using Weights of Evidence and Statistical Index Models. *Sustainability* **2022**, *14*, 3881. [[CrossRef](#)]
14. Malik, A.; Rao, M.R.; Puppala, N.; Kooruri, P.; Thota, V.A.K.; Liu, Q.; Chiao, S.; Gao, J. Data-Driven Wildfire Risk Prediction in Northern California. *Atmosphere* **2021**, *12*, 109. [[CrossRef](#)]
15. Onsterwisch, Z.; Maunteland, A.; Nisbett, N.; Dibbya, D.; Alsharova, A. Particulate Matter Detection in Mines Using 3D Light Detection and Ranging Technology. In Proceedings of the 2023 IEEE Wireless Communications and Networking (WCNC), Glasgow, Scotland, UK, 26–29 March 2023; pp. 1–6.
16. Zhang, L.; Wang, B.; Peng, W.; Li, C.; Lu, Z.; Guo, Y. A Method for Forest Fire Detection Using UAV. *Adv. Sci. Technol. Lett.* **2015**, *81*, 69–74.
17. Alsharova, A.; Yuksel, M. UAV-Direct: Facilitating D2D Communications for Dynamic and Infrastructure-less Networking. In Proceedings of the 4th ACM Workshop on Micro Aerial Vehicle Networks, Systems, and Applications, Mobile Systems, Applications, and Services (MobiSys), Munich, Germany, 10–15 June 2018; pp. 57–62.
18. Selim, M.Y.; Alsharova, A.; Kamal, A.E. Short-Term and Long-Term Cell Outage Compensation Using UAVs in 5G Networks. In Proceedings of the 2018 IEEE Global Communications Conference (GLOBECOM), Abu Dhabi, United Arab Emirates, 9–13 December 2018; pp. 1–6.
19. Alsharova, A.; Ghazzai, H.; Yuksel, M.; Kadri, A.; Kamal, A.E. Trajectory Optimization for Multiple UAVs Acting as Wireless Relays. In Proceedings of the 2018 IEEE International Conference on Communications Workshops (ICC Workshops), Kansas City, MO, USA, 20–24 May 2018; pp. 1–6.
20. Nait-Abdesselam, F.; Alsharova, A.; Selim, M.Y.; Qiao, D.; Kamal, A.E. Towards enabling unmanned aerial vehicles as a service for heterogeneous applications. *J. Commun. Netw.* **2021**, *23*, 212–221. [[CrossRef](#)]
21. Osterwisch, Z.; Rinchi, O.; Alsharova, A.; Ghazzai, H.; Massoud, Y. Multiple UAV-LiDAR Placement Optimization Under Road Priority and Resolution Requirements. In Proceedings of the 2023 IEEE International Conference on Communications (ICC), Rome, Italy, 28 May–1 June 2023; pp. 1–6.
22. Yuan, C.; Liu, Z.; Zhang, Y. Aerial Images-Based Forest Fire Detection for Firefighting Using Optical Remote Sensing Techniques and Unmanned Aerial Vehicles. *J. Intell. Robot. Syst.* **2017**, *88*, 635–654. [[CrossRef](#)]
23. Allison, R.S.; Johnston, J.M.; Craig, G.; Jennings, S. Airborne Optical and Thermal Remote Sensing for Wildfire Detection and Monitoring. *Sensors* **2016**, *16*, 1310. [[CrossRef](#)] [[PubMed](#)]
24. Kinaneva, D.; Hristov, G.V.; Raychev, J.; Zahariev, P. Early Forest Fire Detection Using Drones and Artificial Intelligence. In Proceedings of the 2019 42nd International Convention on Information and Communication Technology, Electronics and Microelectronics (MIPRO), Opatija, Croatia, 20–24 May 2019; pp. 1060–1065.
25. Yuan, C.; Liu, Z.; Zhang, Y. Fire detection using infrared images for UAV-based forest fire surveillance. In Proceedings of the 2017 International Conference on Unmanned Aircraft Systems (ICUAS), Miami, FL, USA, 13–16 June 2017; pp. 567–572.
26. Rjoub, D.; Alsharova, A.; Masadeh, A. Early Wildfire Detection using UAVs Integrated with Air Quality and LiDAR Sensors. In Proceedings of the 2022 IEEE 96th Vehicular Technology Conference (VTC2022-Fall), London, UK, 26–29 September 2022; pp. 1–5.
27. Gottuk, D.T.; Peatross, M.J.; Roby, R.J.; Beyler, C.L. Advanced fire detection using multi-signature alarm algorithms. *Fire Saf. J.* **2002**, *37*, 381–394. [[CrossRef](#)]
28. Wang, X.; Zhou, H.; Arnott, W.P.; Meyer, M.E.; Taylor, S.; Firouzkouhi, H.; Moosmüller, H.; Chow, J.C.; Watson, J.G. Evaluation of gas and particle sensors for detecting spacecraft-relevant fire emissions. *Fire Saf. J.* **2020**, *113*, 102977. [[CrossRef](#)]
29. Gutmacher, D.; Hofer, U.; Wöllenstein, J. Gas sensor technologies for fire detection. *Sens. Actuators B Chem.* **2012**, *175*, 40–45. [[CrossRef](#)]
30. Mehadi, A.; Moosmüller, H.; Campbell, D.; Ham, W.; Schweizer, D.; Tarnay, L.; Hunter, J. Laboratory and field evaluation of real-time and near real-time PM2.5 smoke monitors. *J. Air Waste Manag. Assoc.* **2019**, *70*, 158–179. [[CrossRef](#)] [[PubMed](#)]
31. Illingworth, S.; Allen, G.; Percival, C.; Hollingsworth, P.; Gallagher, M.; Ricketts, H.; Hayes, H.; Ładosz, P.; Crawley, D.; Roberts, G. Measurement of boundary layer ozone concentrations on-board a Skywalker unmanned aerial vehicle. *Atmos. Sci. Lett.* **2014**, *15*, 252–258. [[CrossRef](#)]
32. Rhode, S. *Drone Search-and-Rescue Study Reveals Potential, Limits*; Aircraft Owners and Pilots Association: Frederick, MD, USA, 2018.
33. Reisen, F.; Meyer, C.; Weston, C.; Volkova, L. Ground-Based Field Measurements of PM2.5 Emission Factors From Flaming and Smoldering Combustion in Eucalypt Forests. *J. Geophys. Res. Atmos.* **2018**, *123*, 8301–8314.
34. David, C.C.; Alley, F.C. *Air Pollution Control: A Design Approach*; Waveland Press Inc.: Long Grove, IL, USA, 2010.

35. Al-Hourani, A.; Kandeepan, S.; Jamalipour, A. Modeling air-to-ground path loss for low altitude platforms in urban environments. In Proceedings of the 2014 IEEE Global Communications Conference (GLOBECOM), Austin, TX, USA, 8–12 December 2014; pp. 2898–2904.
36. Hourani, A.; Sithamparanathan, K.; Lardner, S. Optimal LAP altitude for maximum coverage. *IEEE Wirel. Commun. Lett.* **2014**, *3*, 569–572. [[CrossRef](#)]
37. Holis, J.; Pechac, P. Elevation dependent shadowing model for mobile communications via high altitude platforms in built-up areas. *IEEE Trans. Antennas Propag.* **2008**, *56*, 1078–1084. [[CrossRef](#)]
38. Cotton, S.L. Human Body Shadowing in Cellular Device-to-Device Communications: Channel Modeling Using the Shadowed $\kappa - \mu$ Fading Model. *IEEE J. Sel. Areas Commun.* **2015**, *33*, 111–119. [[CrossRef](#)]
39. Obayashi, S.; Zander, J. A body-shadowing model for indoor radio communication environments. *IEEE Trans. Antennas Propag.* **1998**, *46*, 920–927. [[CrossRef](#)]
40. Zheng, Y.; Wang, Y.; Meng, F. Modeling and simulation of pathloss and fading for air-ground link of HAPs within a network simulator. In Proceedings of the 2013 IEEE International Conference on Cyber-Enabled Distributed Computing and Knowledge Discovery (CyberC), Beijing, China, 10–12 October 2013.
41. Zeng, Y.; Zhang, R. Energy-Efficient UAV Communication With Trajectory Optimization. *IEEE Trans. Wirel. Commun.* **2017**, *16*, 3747–3760. [[CrossRef](#)]
42. Hulens, D.; Verbeke, J.; Goedemé, T. Choosing the best embedded processing platform for on-board UAV image processing. In Proceedings of the 10th International Joint Conference on Computer Vision, Imaging and Computer Graphics, Berlin, Germany, 11–14 March 2015; Springer: Cham, Switzerland, 2015; pp. 455–472.
43. Liu, X.; Yu, X.; Zhang, Z. PM2.5 concentration differences between various forest types and its correlation with forest structure. *Atmosphere* **2015**, *6*, 1801–1815. [[CrossRef](#)]
44. Charland, A.; Clements, C. Kinematic structure of a wildland fire plume observed by Doppler LiDAR. *IEEE/ACM Trans. Netw.* **2013**, *118*, 3200–3212. [[CrossRef](#)]
45. Boyd, S.; Vandenberghe, L. *Convex Optimization*; Cambridge University Press: New York, NY, USA, 2004.
46. Mitchell, M. *An Introduction to Genetic Algorithms*; MIT Press: Cambridge, MA, USA, 1998.
47. Beasley, D.; Bull, D.R.; Martin, R.R. An Overview of Genetic Algorithms: Part 2, Research Topics. *Univ. Comput.* **1993**, *15*, 170–181.
48. Wotton, B.; Gould, J.; McCaw, L.; Cheney, P.; Taylor, S. Flame temperature and residence time of fires in dry eucalypt forest. *Int. J. Wildland* **2012**, *22*, 270–281. [[CrossRef](#)]
49. Alsharoa, A.; Ghazzai, H.; Kadri, A.; Kamal, A.E. Spatial and Temporal Management of Cellular HetNets with Multiple Solar Powered Drones. *IEEE Trans. Mob. Comput.* **2020**, *19*, 954–968. [[CrossRef](#)]
50. Boyd, S.; Mutapcic, A. *Stochastic Subgradient Methods*; Notes for EE364; Stanford University: Stanford, CA, USA, 2006.

Disclaimer/Publisher’s Note: The statements, opinions and data contained in all publications are solely those of the individual author(s) and contributor(s) and not of MDPI and/or the editor(s). MDPI and/or the editor(s) disclaim responsibility for any injury to people or property resulting from any ideas, methods, instructions or products referred to in the content.